

Study of neutron-induced background and its impact on the search of $0\nu\beta\beta$ decay in ^{124}Sn

N. Dokania^{a,b}, V. Singh^{a,b}, S. Mathimalar^{a,b}, C. Ghosh^c, V. Nanal^{c*}, R.G. Pillay^c, S. Pal^c, K.G. Bhushan^d and A. Shrivastava^e

^a*India-based Neutrino Observatory,*

Tata Institute of Fundamental Research, Mumbai 400 005, India

^b*Homi Bhabha National Institute,*

Anushaktinagar, Mumbai 400 094, India

^c*Department of Nuclear and Atomic Physics, Tata Institute of Fundamental Research, Colaba, Mumbai 400 005, India*

^d*Technical Physics Division, Bhabha Atomic Research Centre, Mumbai 400 085, India*

^e*Nuclear Physics Division, Bhabha Atomic Research Centre, Mumbai 400 085, India*

E-mail: nanal@tifr.res.in

ABSTRACT: Neutron-induced background has been studied in various components of the TIN.TIN detector, which is under development for the search of Neutrinoless Double Beta Decay in ^{124}Sn . Fast neutron flux $\sim 10^6 \text{ n cm}^{-2}\text{s}^{-1}$ covering a broad energy range (~ 0.1 to ~ 18 MeV) was generated using $^9\text{Be}(p,n)^9\text{B}$ reaction. In addition, reactions with quasi-monoenergetic neutrons were also studied using $^7\text{Li}(p,n)^7\text{Be}$ reaction. Among the different cryogenic support structures studied, Teflon is found to be preferable compared to Torlon as there is no high energy gamma background ($E_\gamma > 1$ MeV). Contribution of neutron-induced reactions in $^{\text{nat},124}\text{Sn}$ from other Sn isotopes ($A = 112 - 122$) in the energy region of interest, namely, around the $Q_{\beta\beta}$ of ^{124}Sn ($E \sim 2.293$ MeV), is also investigated.

KEYWORDS: Gamma detectors, Double-beta decay detectors.

*Corresponding author.

Contents

1. Introduction	1
2. Experimental Details	2
3. Data Analysis and Results	4
3.1 Neutron-induced activity from Torlon and Teflon	6
3.2 Neutron-induced activity from $^{\text{nat}}\text{Pb}$ and $^{\text{nat}}\text{Cu}$	8
3.3 Neutron-induced activity in $^{\text{nat}}\text{Sn}$ and ^{124}Sn	10
3.4 Impact of neutron-induced gamma background for $0\nu\beta\beta$ decay in ^{124}Sn	12
3.4.1 Estimation of neutron flux	12
3.4.2 Estimation of neutron-induced gamma background for $E_\gamma \geq 2.1$ MeV	13
4. Conclusions	14

1. Introduction

For rare event studies like Double Beta Decay (DBD) and dark matter searches, the reduction of background is very important for improving the sensitivity of the experiment. Typical half-life for DBD process, $T_{1/2} > 10^{18}$ years [1], is much larger than that of natural radioactivity from U, Th chains and ^{40}K ($T_{1/2} \sim 10^8 - 10^{10}$ years). In recent years, ultra-low levels of background $< 10^{-2}$ counts/(keV kg yr) have been reported in rare decay event experiments [2, 3]. The background level in an underground laboratory is mainly limited by trace impurities present in detector materials, which can be minimized but cannot be eliminated completely. Of the different sources of background, namely, α, β, γ and neutrons, background arising from neutrons is most difficult to suppress and hence crucial to understand. In fact, Kim et al. [4] have reported neutrons to be the limiting source of background for dark matter search experiment KIMS (Korean Invisible Mass Search). Neutrons are produced in the spontaneous fission of $^{\text{nat}}\text{U}$ (mainly ^{238}U), Th present in the rocks and the surrounding materials. In addition, alpha particles produced from decay of intermediate nuclei in the natural decay chains can react with light nuclei in the rocks to produce neutrons via (α, n) reactions [5]. Very high energy neutrons ($E_n \sim \text{GeV}$) are produced by muon-induced interactions in the rocks and materials surrounding the detector. It has been reported that in an underground laboratory, the low energy neutron flux ($E_n < 10$ MeV) from natural radioactivity is about two to three orders of magnitude higher than that from the muon-induced reactions [4–7]. Although the high energy neutrons are more penetrating, the average neutron energy reduces from 100 – 200 MeV to ~ 45 MeV [8] as they propagate through layers of shield materials. Thus, it is important to understand the background arising from low energy neutrons. It should be mentioned that active veto systems are employed for the rejection of muon-induced events in the shield

and detector/source assembly [9], while the flux of the low energy neutrons is reduced by suitable shielding (mostly hydrogenous materials) around the detector [10]. With low energy neutrons, the inelastic scattering of neutrons ($n, n'\gamma$) and neutron-capture (n, γ) with the source/detector and the surrounding materials are main sources of gamma background. In addition, any impurities in these materials could be potential sources of neutron-induced background. The reaction products formed upon neutron activation can have half-lives ranging from \sim min to \sim years. The short-lived activities can be avoided by storing the material for prolonged periods in underground locations but the long-lived activities are highly undesirable.

In India, TIN.TIN detector (The INDia-based TIN detector) comprising cryogenic bolometer array of Tin detector elements is under development for a feasibility study to search for $0\nu\beta\beta$ decay in ^{124}Sn [11, 12]. It is essential to understand the gamma background in the region of interest (ROI) near $Q_{\beta\beta}$, which for ^{124}Sn is 2292.64 ± 0.39 keV [13]. With this motivation, the neutron-induced background ($E_n < 20$ MeV) in TIN.TIN detector components is investigated. The aim of the neutron activation study ($E_n < 20$ MeV) is two fold – the selection of materials suitable for use in and around the cryogenic bolometer and the evaluation of its impact on the gamma background level. The paper is organized as follows: Section 2 describes the experimental details, while data analysis and results are presented in Section 3. Conclusions are discussed in Section 4.

2. Experimental Details

The TIN.TIN detector will consist of $^{\text{nat}}\text{Sn}$ or ^{124}Sn bolometer mounted in a specially designed low background cryostat. The neutron-induced gamma background from the cryostat housing can be significantly reduced by mounting low activity Pb shield inside the cryostat (similar to CUORE [14]). Hence, only the neutron activation of materials in the close vicinity of the detectors elements is of prime importance. For neutron-induced background study the materials chosen are: high purity ETP (Electrolytic Tough Pitch) $^{\text{nat}}\text{Cu}$ (2N purity) used inside the cryostat; Torlon (4203), Torlon (4301) and Teflon – cryogenic materials for detector holders; $^{\text{nat}}\text{Pb}$ – the common shielding material, $^{\text{nat}}\text{Sn}$ (7N purity) and 97.2% enriched ^{124}Sn . Torlon 4203, 4301 and Teflon samples used were of standard commercial grade. Elemental concentrations were obtained using Time of Flight Secondary Ion Mass Spectrometry (TOF-SIMS). Since all the materials contain high percentage of ^{19}F , Secondary Ion Mass Spectra were obtained in both positive and negative ion modes to ascertain the total fluorine concentration. Final elemental concentrations were obtained after suitable correction with weighted relative sensitivity factors (RSF) for individual element [15] and is given in table 1. Besides C, F and O, the major elements found in Torlon 4203 is Ti (contains TiO_2 [16]) while Fe was found in Torlon 4301, which could be undesirable for low temperature applications. The samples also showed additional trace elements like Si, S, Cl and Mn but only dominant components with concentration $> 0.1\%$ are listed in table 1.

The neutron activation was performed using proton beam on Be and Li production targets in the neutron irradiation setup at the Pelletron Linac Facility, Mumbai [17]. Irradiation targets were mounted in a forward direction with respect to the proton beam, close to the production target but outside the vacuum chamber. This facilitated the change of irradiation targets without breaking the accelerator vacuum. The setup is located in a well shielded area above the analyzing magnet of the Pelletron, which permits the use of high proton beam current ~ 120 nA on the production target.

Table 1. Elemental distribution of Torlon 4203, Torlon 4301 and Teflon obtained with SIMS.

Element	Torlon 4203	Torlon 4301	Teflon
	(%)	(%)	(%)
^{12}C	28	27	24.4
^{16}O	1.2	1.3	0.9
^{19}F	66.2	67	72.3
^{23}Na	0.1	0.2	0.2
$^{24,25,26}\text{Mg}$	0.2	0.3	0.3
^{27}Al	0.2	0.2	0.2
^{31}P	0.2	0.2	0.2
$^{39,40,41}\text{K}$	0.2	0.2	0.2
^{40}Ca	0.1	0.5	0.1
$^{46,47,48,49,50}\text{Ti}$	2.1	0.7	0.2
$^{50,52,53,54}\text{Cr}$	0.3	0.1	0.1
$^{54,56,57,58}\text{Fe}$	0.5	1.1	0.1
$^{58,60,61,62}\text{Ni}$	0.1	0.5	0.1
$^{63,65}\text{Cu}$	0.2	0.3	0.3

In the present study, proton beams of energy $E_p = 10\text{-}20$ MeV on a Be target (5 mm thick) were used to obtain neutrons of a broad energy range with reaction $^9\text{Be}(p,n)^9\text{B}$ ($Q = -1.850$ MeV) [18]. Beam energies were chosen to cover the energy range of neutron spectra originating from fission and (α, n) reactions in the rocks [5]. The energy dependence of the cross-sections of the possible reaction channels in different targets was also taken into consideration. In addition, nearly mono-energetic neutrons were produced with the $^7\text{Li}(p,n)^7\text{Be}$ ($Q = -1.644$ MeV) reaction by bombarding a 0.15 mm thick natural Lithium target (wrapped in a ~ 2 μ thick Ta foil) with proton beam of energy 12 MeV. Contribution from the ^6Li (natural abundance 7.59%) in the natural lithium target is expected to be negligible. At $E_p = 12$ MeV, due to the contributions from the excited states of ^7Be , quasi-monoenergetic neutrons are produced [19,20]. The flux obtained in case of the Li target was smaller than that in the case of Be by a factor of ~ 10 . However, the better definition of neutron energy was useful for identification of some of the reaction channels. It should be mentioned that neutron flux could not be measured accurately in the setup and hence $^{\text{nat}}\text{Fe}$ target ($\sim 5 - 6$ mg/cm²) was used to estimate neutron flux with the $^{56}\text{Fe}(n,p)^{56}\text{Mn}$ reaction. Multiple irradiation targets (upto five) were stacked in a 3 cm long target holder (Aluminum or Teflon) using Teflon spacers for an efficient utilization of beam time. In this geometry, the solid angles subtended by the neutron beam at the first and last target were ~ 0.25 sr and ~ 0.04 sr, respectively. Thickness of irradiated targets varied from 1.8 mg/cm² to 0.29 g/cm². Both short (2 – 3 h) as well as long (10 – 35 h) duration irradiation were carried out to look for short-lived and long-lived products. In case of long irradiation experiments, the access to target area was restricted due to the radiation safety limits and targets could be taken out for measurements only after sufficient cooling time (~ 20 min to ~ 1 h). Hence, some of the short-lived activities could not be observed.

The irradiated targets were counted offline for the detection of characteristic γ -rays of reaction products resulting from neutron activation. Three counting setups with efficiency calibrated HPGe

detectors were used. One setup consisted of a low background detector of relative efficiency (R.E.) $\sim 70\%$ with a 10 cm low activity Pb ($^{210}\text{Pb} < 0.3 \text{ Bq/kg}$) and 5 cm low activity Cu shield [21]. The other two HPGe detectors of R.E. $\sim 30\%$ (D1 and D2) were shielded with 5 cm thick normal Pb rings. D1 and D2 were mostly used for identification of gamma-rays and half-life measurements. Targets were mounted in a close geometry in these counting setups to search for low levels of activity and coincident summing effects had to be taken into account. Data were recorded with a commercial FPGA based 100 MS/s digitizer (CAEN-N6724) [22] and analyzed using LAMPS [23]. It should be mentioned that all targets were studied in the low background setup prior to irradiation and did not show any radioactivity above the background level.

3. Data Analysis and Results

Table 2 lists the details of the products formed in different samples together with their half-lives and the expected γ -rays. The last two columns of the table 2 show the minimum neutron energy E_n at which the cross-section for the respective neutron-induced reaction channel is $\geq \mu\text{b}$. In most of the cases, the half-life ($T_{1/2}$) of the reaction products were measured and were found to agree within 20% of the reference values [24]. The gamma-rays with energies within the ROI of $0\nu\beta\beta$ decay in ^{124}Sn , that is, within $\pm 200 \text{ keV}$ of $Q_{\beta\beta}$ as well as with $E \geq Q_{\beta\beta}$ are potential sources of background and are highlighted in bold text in table 2. It should be mentioned that many of these reaction products decay by β^- emission and if the $Q_\beta \geq$ than the $Q_{\beta\beta}(^{124}\text{Sn})$, electrons or bremsstrahlung resulting from these electrons can contribute to the background in ROI. Due to short range of electrons, contribution to the background in the detector arising due to β -decays in the shield and support materials will be mainly from the surface events. This together with β -decays within the detector will affect the background, which is not considered in the present work.

Table 2. Neutron-induced reaction products, $T_{1/2}$ and expected γ -rays in the irradiated samples. The minimum neutron energy E_n at which corresponding σ is $\geq \mu\text{b}$ is also listed [24].

Sample	Reaction channel	$T_{1/2}$	E_γ (keV)	E_n (MeV)	σ (barn)
Torlon 4203	$^{\text{nat}}\text{Ti}(n, X)^{47}\text{Sc}$	3.3492 d	159.4		
	$^{\text{nat}}\text{Ti}(n, X)^{48}\text{Sc}$	43.67 h	175.4, 983.5 1037.5, 1312.1		
	$^{\text{nat}}\text{Ti}(n, X)^{46}\text{Sc}$	83.79 d	889.3, 1120.5		
	$^{27}\text{Al}(n, \alpha)^{24}\text{Na}$	14.997 h	1368.6, 2754.0	4.6	1.4×10^{-6}
	$^{27}\text{Al}(n, p)^{27}\text{Mg}$	9.458 min	843.8, 1014.5	2.5	1.9×10^{-5}
Torlon 4301	$^{56}\text{Fe}(n, p)^{56}\text{Mn}$	2.5789 h	846.8, 1810.7 2113.1	4	6.0×10^{-6}
	$^{27}\text{Al}(n, \alpha)^{24}\text{Na}$	14.997 h	1368.6, 2754.0	4.6	1.4×10^{-6}
Teflon	$^{19}\text{F}(n, 2n)^{18}\text{F}$	109.77 min	511	11.5	1.5×10^{-3}
$^{\text{nat}}\text{Pb}$	$^{204}\text{Pb}(n, 2n)^{203}\text{Pb}$	51.92 h	279.2, 401.3, 680.5	8.5	2.1×10^{-3}
	$^{204}\text{Pb}(n, n')^{204\text{m}}\text{Pb}$	66.93 min	374.8, 899.2, 911.7, 1274	1.0	2.4×10^{-1}
	$^{121}\text{Sb}(n, \gamma)^{122}\text{Sb}$	2.7238 d	564.2, 692.7	0.1	2.1×10^{-1}
	$^{123}\text{Sb}(n, \gamma)^{124}\text{Sb}$	60.20 d	602.7, 1690.9 2090.9, 2182.6, 2294.0	0.1	1.9×10^{-1}
$^{\text{nat}}\text{Cu}$	$^{63}\text{Cu}(n, \gamma)^{64}\text{Cu}$	12.701 h	511, 1345.8	0.055	2.5×10^{-2}
	$^{63}\text{Cu}(n, \alpha)^{60}\text{Co}$	1925.28 d	1173.2, 1332.5	2.5	1.1×10^{-2}
	$^{65}\text{Cu}(n, \gamma)^{66}\text{Cu}$	5.120 min	1039.2	0.06	1.1×10^{-2}
	$^{65}\text{Cu}(n, \alpha)^{62\text{m}}\text{Co}$	13.91 min	1163.5, 1172.9, 2003.7 2104.9, 2301.9, 2882.3	5	3.9×10^{-6}
	$^{65}\text{Cu}(n, p)^{65}\text{Ni}$ $^{64}\text{Ni}(n, \gamma)^{65}\text{Ni}$	2.5175 h	1115.5, 1481.8, 1623.4, 1724.9	2.5 0.553	1.0×10^{-6} 6.5×10^{-3}
$^{\text{nat}, 124}\text{Sn}$	$^{112}\text{Sn}(n, np)^{111}\text{In}$	2.8047 d	171.3, 245.4	12	4.9×10^{-6}
	$^{116}\text{Sn}(n, np)^{115\text{m}}\text{In}$			14.5	7.6×10^{-5}
	$^{115}\text{Sn}(n, p)^{115\text{m}}\text{In}$	4.486 h	336.2	5	1.9×10^{-4}
	$^{115}\text{In}(n, n')^{115\text{m}}\text{In}$			0.5	6.4×10^{-3}
	$^{116}\text{Sn}(n, p)^{116\text{m}}\text{In}$	54.29 min	416.9, 818.7, 1097.3 1293.6, 2112.3	8	1.5×10^{-4}
	$^{117}\text{Sn}(n, n')^{117\text{m}}\text{Sn}$			0.2	2.9×10^{-1}
	$^{116}\text{Sn}(n, \gamma)^{117\text{m}}\text{Sn}$	13.76 d	156.0, 158.6	0.1	5.5×10^{-2}
	$^{118}\text{Sn}(n, 2n)^{117\text{m}}\text{Sn}$			9.9	7.2×10^{-2}
	$^{124}\text{Sn}(n, 2n)^{123\text{m}}\text{Sn}$	40.06 min	160.3	9 0.3	1.6×10^{-1} 1.2×10^{-2}
	$^{122}\text{Sn}(n, \gamma)^{123\text{m}}\text{Sn}$				
	$^{124}\text{Sn}(n, 2n)^{123}\text{Sn}$	129.2 d	1088.6	9 0.3	1.6×10^{-1} 1.2×10^{-2}
	$^{122}\text{Sn}(n, \gamma)^{123}\text{Sn}$				
	$^{124}\text{Sn}(n, \gamma)^{125\text{m}}\text{Sn}$	9.52 min	331.9		
	$^{124}\text{Sn}(n, \gamma)^{125}\text{Sn}$	9.64 d	822.5, 1067.1, 1089.2	0.315	6.8×10^{-3}

3.1 Neutron-induced activity from Torlon and Teflon

Figure 1 shows the γ -ray spectra of the irradiated Torlon 4203, Torlon 4301 and Teflon samples at different times (t_c) after the neutron irradiation. Both Torlon 4203 and 4301 samples were exposed to similar neutron dose, while the neutron dose received by the Teflon sample was $\sim 40\%$ lower. It can be seen that the most dominant gamma-ray is 511 keV in all the three samples, but the Torlon and Teflon samples show different levels of activity and different impurities. The Teflon and Torlon samples contain fluorocarbon in different proportions, which is reflected in the intensity of the 511 keV γ -ray with Teflon having the maximum intensity.

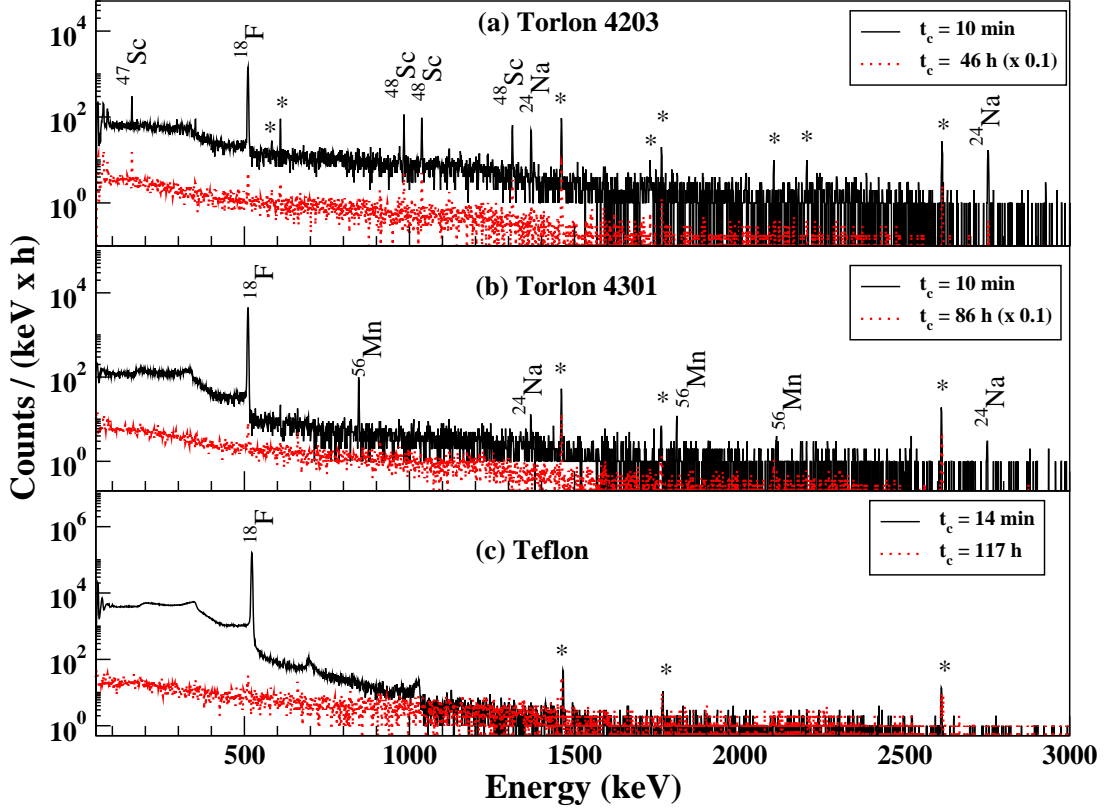


Figure 1. (Color online) γ -ray spectra of the irradiated (a) Torlon 4203 with $E_p = 20$ MeV, $t_{irr} = 3$ h, $N_n \sim 1.31(9) \times 10^{10}$, (b) Torlon 4301 with $E_p = 20$ MeV, $t_{irr} = 3$ h, $N_n \sim 1.38(9) \times 10^{10}$ and (c) Teflon with $E_p = 20$ MeV, $t_{irr} = 2$ h, $N_n \sim 0.82(6) \times 10^{10}$ for different t_c – time elapsed since the end of irradiation. The spectrum shown in (a) is measured in the D2 setup while spectra in (b) and (c) are recorded in the D1 setup. In panels (a) and (b), spectra for larger t_c are scaled by 0.1 for better visualization. The γ -rays originating from room background are indicated with stars.

As mentioned earlier, the Torlon 4203 contains TiO_2 (table 1) and many gamma-rays originating from $\text{Ti}(n, X)\text{Sc}$ reactions are clearly visible (see table 2). Most of the Sc isotopes formed are short-lived and produce γ -rays with $E_\gamma < 1312$ keV. However, ^{46}Sc has a relatively long half-life, namely, $T_{1/2} = 83.79$ d. It may be mentioned that the Large Underground Xenon (LUX) dark matter experiment has observed background from ^{46}Sc , which was formed due to the cosmogenic activation of the LUX Titanium cryostat [27, 28]. In case of the Torlon 4301, γ -rays resulting

from $^{56}\text{Fe}(n,p)^{56}\text{Mn}$ reaction were observed (see figure 1(b)). Both the Torlon samples have traces of Al, which gives rise to γ -ray of energy 2754.0 keV (which is higher than $Q_{\beta\beta}(^{124}\text{Sn})$) with a $T_{1/2} = 14.99$ h and is highly undesirable. Figure 2 shows the decay curves for 511 keV γ -ray in the irradiated Torlon and Teflon samples. The background rate at 511 keV in the different detector systems has been taken into account. The origin of 511 keV from the $^{19}\text{F}(n,2n)^{18}\text{F}$ reaction is confirmed since the measured half-life agrees with that of ^{18}F within errors, namely, $T_{1/2}^{\text{ref}} = 109.77(5)$ min [24].

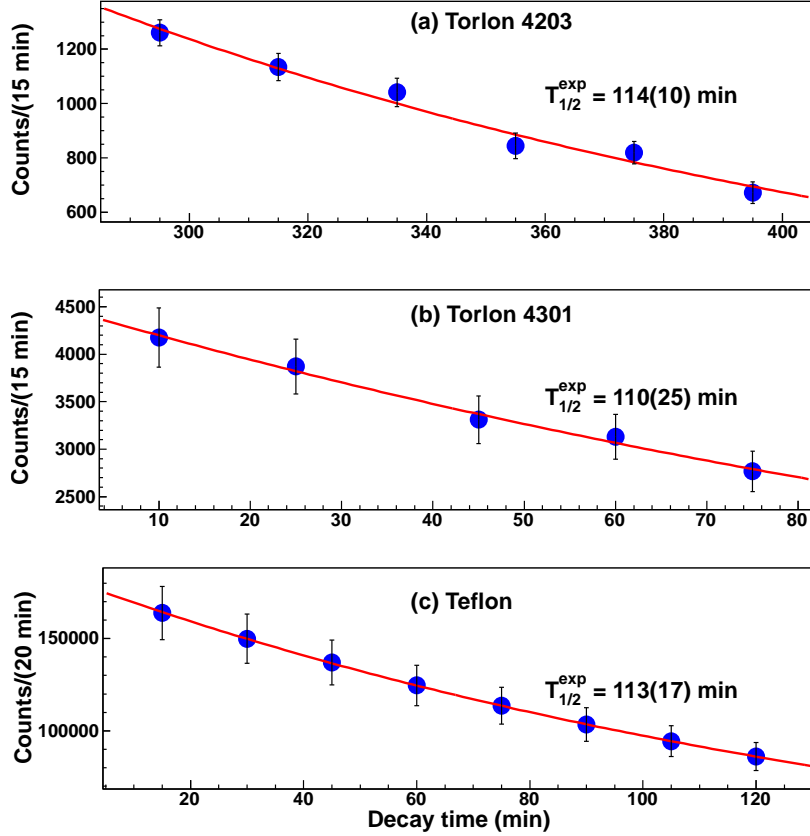


Figure 2. (Color online) Decay curves for 511 keV γ -ray of ^{18}F formed in the irradiated (a) Torlon 4203 with $E_p = 20$ MeV and $t_{\text{irr}} = 10$ h, (b) Torlon 4301 with $E_p = 20$ MeV and $t_{\text{irr}} = 3$ h and (c) Teflon with $E_p = 20$ MeV and $t_{\text{irr}} = 2$ h.

Considering the threshold energy $E_n \sim 11.5$ MeV for $^{19}\text{F}(n,2n)^{18}\text{F}$ reaction [24], this channel is not expected to be activated at lower neutron energies. The γ -ray spectra of irradiated samples at $E_p = 12$ MeV are shown in figure 3 for Teflon (in dotted red lines) and in figure 4 for the Torlon samples. It can be clearly seen that the ^{18}F is not populated at $E_n \leq 9.9$ MeV ($E_p = 12$ MeV) and yield of 511 keV γ -ray is significantly reduced, whereas most of the reaction channels in Torlon are populated even at lower neutron energy (see table 2). It may be mentioned that the observed peaks at 1022 keV and ~ 685.6 keV in the Teflon spectrum, originate from summing of two 511 keV γ -rays and from summing of 511 keV with backscattered gamma-rays, respectively. This is also seen in the $^{\text{nat}}\text{Cu}$ sample.

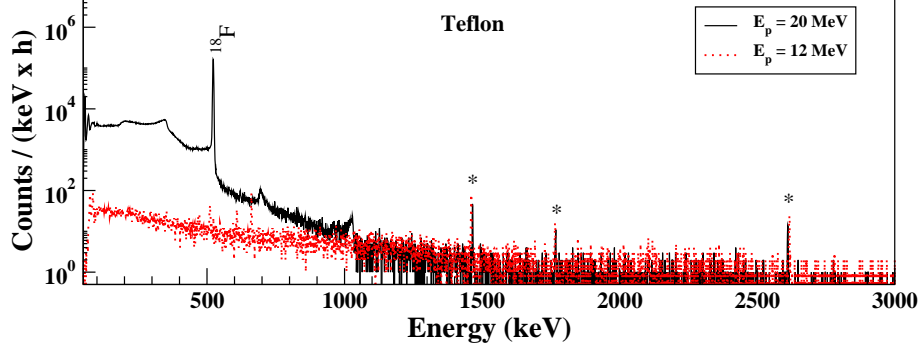


Figure 3. (Color online) γ -ray spectra of the irradiated Teflon with $E_p = 20$ MeV, $t_{irr} = 2$ h and $N_n \sim 0.82(6) \times 10^{10}$ (shown by solid black lines) together with $E_p = 12$ MeV, $t_{irr} = 13$ h and $N_n \sim 1.27(9) \times 10^{10}$ (shown by dotted red lines). Both the spectra have been measured after similar cooling time (t_c) 14 min and 10 min, respectively, in the D1 setup. Stars have same meaning as in figure [1].

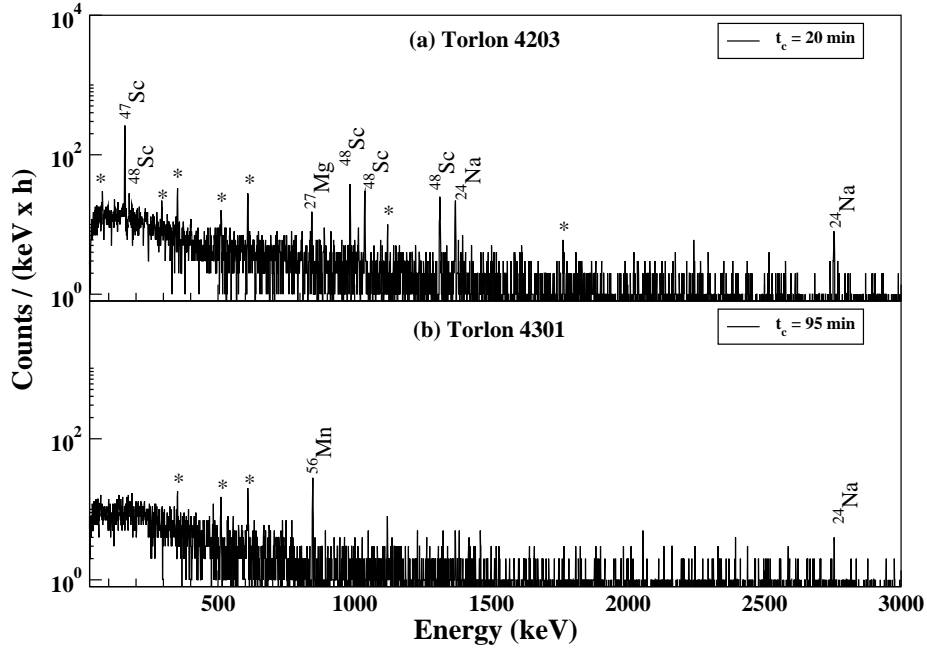


Figure 4. (Color online) γ -ray spectra of the irradiated (a) Torlon 4203 ($N_n \sim 1.4(1) \times 10^{10}$) and (b) Torlon 4301 ($N_n \sim 1.3(1) \times 10^{10}$) with $E_p = 12$ MeV and $t_{irr} = 13$ h. Both the spectra are recorded in the low background setup. Stars have same meaning as in figure [1].

Even though the 511 keV γ -ray activity in Teflon is significantly larger (~ 15.5 (1.2) times) than that in Torlon 4301, there is no gamma background at energies higher than 511 keV in Teflon. Therefore from the neutron-induced gamma background consideration, Teflon seems to be a better candidate as compared to the Torlon for use in the TIN.TIN detector.

3.2 Neutron-induced activity from ^{nat}Pb and ^{nat}Cu

The Lead shield is generally closer to the detector assembly and the gamma-rays produced by neutron-induced reactions in Lead can deteriorate the background levels. It has been previously

reported in Ref. [8] that inelastic scattering of neutrons in Lead can be a significant source of background for double beta decay experiments. The γ -ray spectra of the irradiated ^{nat}Pb and ^{nat}Cu samples are shown in figures 5 (a) and (b), respectively. Gamma-rays originating from decay of ^{203}Pb and ^{204m}Pb (see table 2) are seen in the spectrum. In addition, Sb impurities are also found in the Lead sample. It should be noted that the decay of ^{124}Sb produces many gamma-rays with energies higher than $Q_{\beta\beta}$ of ^{124}Sn but with small branching fractions: 2294.0 keV (0.0320%), 2323.5 keV (0.00243%), 2455.2 keV (0.0015 %), 2681.9 keV (0.00165%), 2693.6 keV (0.0030 %) and 2807.5 keV (0.00147%) [24]. In the present work, only 602.7 keV is observed in the gamma-ray spectrum above the detection limit of the low background setup. But $E_\gamma = 2294.0$ keV may be a crucial source of background in an underground laboratory with improved sensitivity.

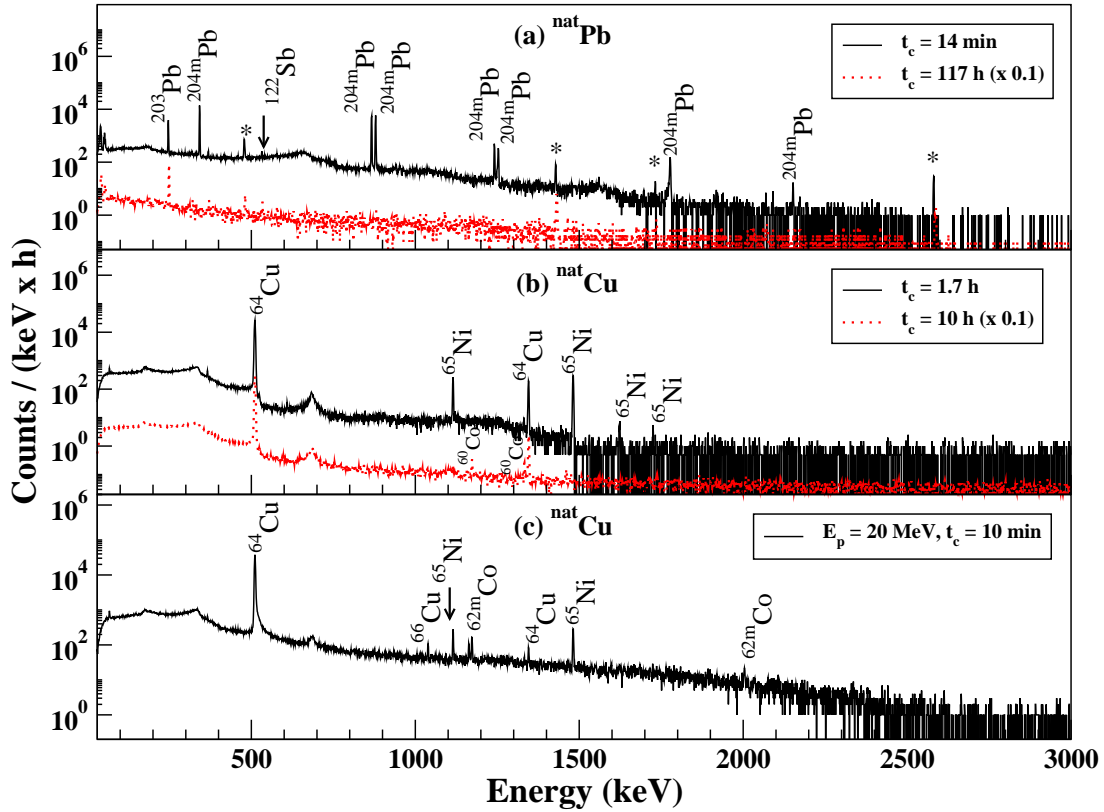


Figure 5. (Color online) γ -ray spectra of the irradiated (a) ^{nat}Pb with $E_p = 20$ MeV, $t_{irr} = 2$ h and $N_n \sim 0.69(5) \times 10^{10}$ for different cooling time t_c , (b) ^{nat}Cu with $E_p = 20$ MeV, $t_{irr} = 10$ h, $N_n \sim 5.9(4) \times 10^{10}$ for different cooling time t_c and (c) ^{nat}Cu with $E_p = 20$ MeV, $t_{irr} = 2$ h and $N_n \sim 1.09(8) \times 10^{10}$. The spectrum shown in (a) is measured in the D2 setup while those in (b) and (c) in the low background setup. In panels (a) and (b), spectra for larger t_c are scaled by 0.1 for better visualization. Stars have same meaning as in figure [1].

In the γ -ray spectrum of ^{nat}Cu (see figure 5(b)) short-lived activities ($T_{1/2} \sim \text{h}$) such as ^{64}Cu and ^{65}Ni are seen. The long-lived products like ^{60}Co ($T_{1/2} = 5.27$ y) are visible in the spectra after sufficient cooling time ~ 10 h, when the overall gamma background level due to the decay of the short-lived nuclei is reduced. Short-lived products ($T_{1/2} \sim \text{min}$) such as ^{62m}Co and ^{66}Cu formed in the Copper sample are visible where spectra could be measured after shorter cooling time.

Figure 6(a) shows decay curve of 511 keV γ -ray in ^{nat}Pb sample indicating $T_{1/2} \sim 41(4)$ min and its origin could not be identified. Whereas the decay curve in figure 6(b) for ^{nat}Cu gives $T_{1/2} \sim 12.4(5)$ h, implying that the 511 keV γ -ray results from the $^{63}\text{Cu}(n, \gamma)^{64}\text{Cu}$ reaction. It should be noted that no ^{18}F was observed in the ^{nat}Pb or ^{nat}Cu samples, confirming that the Teflon sample holder/spacers did not contribute to observed impurities in these samples.

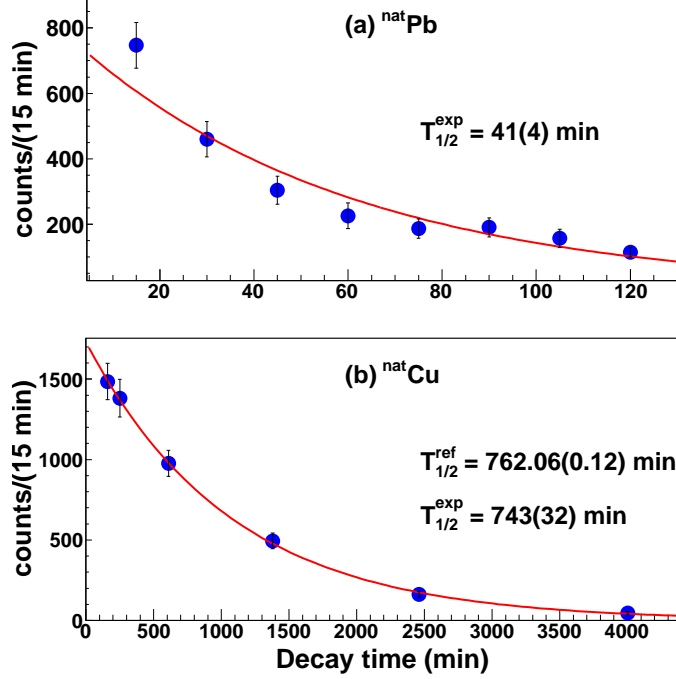


Figure 6. (Color online) Decay curves for 511 keV γ -ray formed in the irradiated (a) ^{nat}Pb with $E_p = 20$ MeV and $t_{irr} = 2$ h, (b) ^{nat}Cu with $E_p = 20$ MeV and $t_{irr} = 2$ h.

Refs. [14, 29] have reported the formation of ^{60}Co in Copper due to cosmogenic activation. In addition, the ^{62m}Co decay produces several high energy γ -rays (see figure 5(c)). Therefore for minimizing the Co activity, it is essential to store Copper in an underground location.

3.3 Neutron-induced activity in ^{nat}Sn and ^{124}Sn

Figure 7(a) shows the γ -ray spectra of the neutron irradiated ($E_{max} = 17.9$ MeV) enriched ^{124}Sn (97.2%) sample. In addition to the gamma-rays originating from neutron activation of ^{124}Sn , reaction products of other Sn isotopes, namely, ^{112}Sn , ^{115}Sn , ^{116}Sn , ^{117}Sn and ^{122}Sn , are also found in the enriched sample (see table 2). Most of the isotopes formed are short-lived, the longest-lived being ^{123}Sn with a $T_{1/2} = 129.2$ d. The highest energy gamma-ray $E_\gamma = 2112.3$ keV originates in the decay of ^{116m}In . Some of the observed reaction products can be produced by different Tin isotopes depending on the incident neutron energy and the relative cross-sections. For example, ^{123m}Sn can be formed either by $^{122}\text{Sn}(n, \gamma)^{123m}\text{Sn}$ or by $^{124}\text{Sn}(n, 2n)^{123m}\text{Sn}$ reaction. The contribution from ^{122}Sn was probed by low energy neutron irradiation ($E_{max} = 7.9$ MeV corresponding to $E_p = 10$ MeV) where the $^{124}\text{Sn}(n, 2n)^{123m}\text{Sn}$ is unfavoured. The observation of significantly reduced

(0.16%) but measurable activity of $^{123\text{m}}\text{Sn}$ ($E_\gamma = 160.3$ keV) at lower neutron energy clearly indicated the traces of ^{122}Sn in the enriched sample. Similarly, $^{115\text{m}}\text{In}$ ($E_\gamma = 336.2$ keV) can be produced from $^{115,116}\text{Sn}$ with high energy neutrons but at lower neutron energy only $^{115}\text{In}(n, n')^{115\text{m}}\text{In}$ (^{115}In natural abundance 95.7%) is the possible reaction channel. Thus, observation of 336.2 keV with low energy neutrons implies presence of trace impurity of ^{115}In in the enriched Tin target. In the observed spectra, γ -rays 1088.6 and 1089.2 keV originating from decay of ^{123}Sn ($T_{1/2} = 129.2$ d) and ^{125}Sn ($T_{1/2} = 9.64$ d), respectively, could not be separated. Measurements after $t_c \sim 10$ d showed that the relative yield of $E_\gamma = 1089.2$ keV was higher than that for $E_\gamma = 1067$ keV confirming the formation of ^{123}Sn . It should be noted that 331.9 keV and 822.5 keV γ -rays from $^{125\text{m}}\text{Sn}$ and ^{125}Sn , respectively, were also visible.

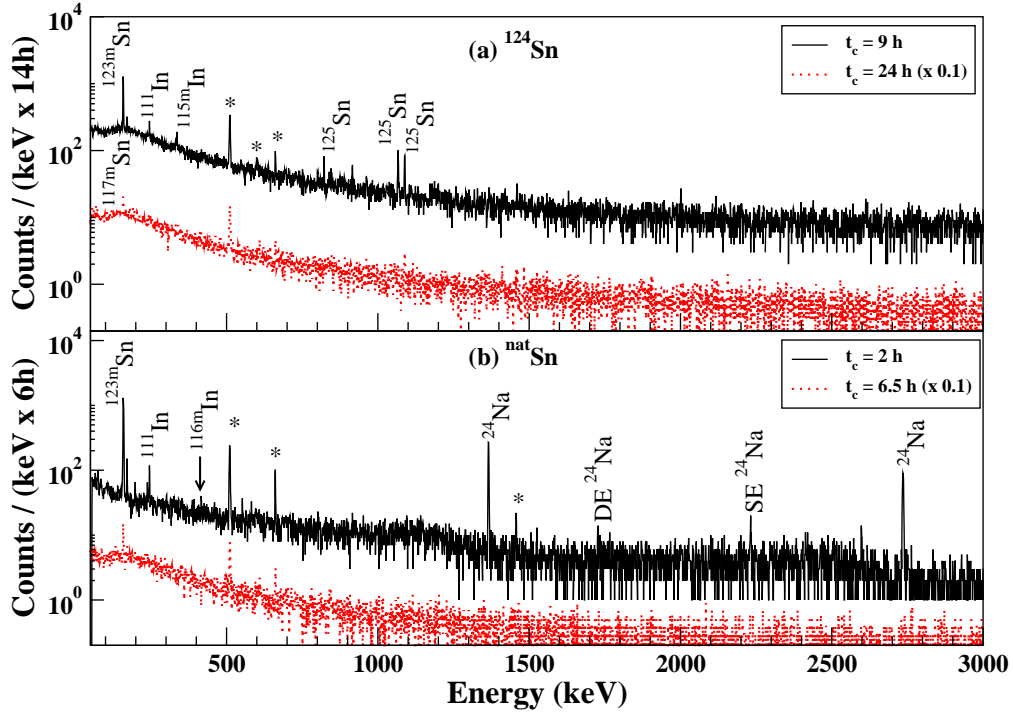


Figure 7. (Color online) γ -ray spectra of the irradiated (a) ^{124}Sn with $E_p = 20$ MeV, $t_{irr} = 10$ h, $N_n \sim 4.1(3) \times 10^{10}$ (solid black lines) and with $E_p = 10$ MeV, $t_{irr} = 5$ h and $N_n \sim 0.44(4) \times 10^{10}$ (dotted red lines), (b) $^{\text{nat}}\text{Sn}$ with $E_p = 20$ MeV, $t_{irr} = 2$ h, $N_n \sim 1.9(1) \times 10^{10}$ (solid black lines) and with $E_p = 10$ MeV, $t_{irr} = 5$ h, $N_n \sim 0.51(4) \times 10^{10}$ (dotted red lines). All spectra are recorded in the low background setup and those corresponding to larger t_c have been scaled by 0.1 for better visualization. Stars have same meaning as in figure [1].

Figure 7(b) shows the γ -ray spectra of irradiated $^{\text{nat}}\text{Sn}$ sample with low energy neutrons, where the gamma-rays from reaction products of ^{112}Sn , ^{116}Sn and ^{122}Sn are visible. The other stable isotopes of Sn upon neutron activation form either long-lived and/or stable reaction products and hence could not be observed. It should be noted that 336.2 keV γ -ray from $^{115\text{m}}\text{In}$ was not visible in the $^{\text{nat}}\text{Sn}$ (7N) sample at the same detection sensitivity as in case of ^{124}Sn . Gamma-rays originating from decay of ^{24}Na was observed in the samples irradiated in an Al target holder, produced via $^{27}\text{Al}(n, \alpha)^{24}\text{Na}$ reaction (see figure 7(b)). No additional impurities are seen in the $^{\text{nat}}\text{Sn}$ (7N)

sample.

3.4 Impact of neutron-induced gamma background for $0\nu\beta\beta$ decay in ^{124}Sn

3.4.1 Estimation of neutron flux

As mentioned earlier, the neutron flux is estimated from the yield of 846.7 keV γ -ray, produced via $^{56}\text{Fe}(n, p)^{56}\text{Mn}$ reaction. Since the neutron spectra produced from the $^9\text{Be}(p, n)^9\text{B}$ reaction is continuous, energy integrated neutron flux has been estimated in the energy range of $E_n \sim 0.1$ MeV to E_{max} , where $E_{max} = E_p - Q_{th}$ with $Q_{th} = 2.057$ MeV.

The number of Mn atoms (N_{Mn}) produced by irradiation of a Fe target with a constant neutron flux ϕ_n ($n \text{ cm}^{-2} \text{ s}^{-1}$) for time t_{irr} is given by,

$$N_{Mn} = \frac{N_{Fe} (1 - e^{-\lambda t_{irr}}) \sum_{E_n} \sigma_c(E_n) \phi_n(E_n) dE_n}{\lambda} \quad (3.1)$$

where N_{Fe} is number of Fe target atoms, λ is the decay constant of ^{56}Mn and $\sigma_c(E_n)$ is the (n, p) cross-section of $^{56}\text{Fe}(n, p)^{56}\text{Mn}$ reaction at the neutron energy E_n . The factor $((1 - e^{-\lambda t_{irr}})/\lambda)$ arises from decay during irradiation.

The N_{Mn} can be obtained from the measured photo peak area (N_γ) of 846.7 keV γ -ray as,

$$N_{Mn} = \frac{N_\gamma}{e^{-\lambda t_c} (1 - e^{-\lambda t}) I_\gamma \varepsilon_\gamma} \quad (3.2)$$

where t_c is the time elapsed between the end of neutron irradiation and start of the counting (cool-down time), t is the counting period, I_γ is the branching ratio and ε_γ is the photo peak detection efficiency of E_γ (846.7 keV) for a finite size source in close geometry, computed from Geant4-based Monte Carlo simulations [21].

Since the distribution of neutrons produced from the $^9\text{Be}(p, n)^9\text{B}$ reaction is continuous, energy integrated neutron flux can be estimated as,

$$\langle \phi_n \rangle = \frac{\sum_{E_n} \sigma_c(E_n) \phi_n(E_n) dE_n}{\sum_{E_n} \sigma_c(E_n) dE_n} \quad (3.3)$$

The numerator in eq. 3.3 is extracted from eq. 3.1 while the denominator is obtained using ENDF/B-VII library [24]. In case of Li target, since the emitted neutrons are nearly monoenergetic, the measured value of neutron capture cross section in the same setup, $\sigma_c = 65.88$ (4.54) barn, at an average neutron energy $E_n = 9.85$ MeV corresponding to $E_p = 12$ MeV is used [25].

Table 3 shows the extracted neutron flux at a distance $d \sim 5$ cm from the production target (Be/Li) for different proton energies together maximum energy of the neutrons E_{max} and average energy of the neutrons $\langle E_n \rangle$. The $\langle E_n \rangle$ for $p+^9\text{Be}$ reaction is calculated as,

$$\langle E_n \rangle = \frac{\sum_{i=0}^3 \sum_{E_n} \sigma_{(p, n_i)}(E_n) E_n dE_n}{\sum_{i=0}^3 \sum_{E_n} \sigma_{(p, n_i)}(E_n) dE_n} \quad (3.4)$$

where the summation runs over E_n from ~ 0.1 MeV to E_{max} and $\sigma_{(p, n_i)}(E_n)$ corresponds to $^9\text{Be}(p, n_i)^9\text{B}$ cross-section at E_n for the i th channel of neutron production [24]. Only (p, n_0) , (p, n_1) , (p, n_2) and (p, n_3) channels are considered and others with total cross-sections $< 6\%$ of (p, n_0) are neglected. The uncertainty in the neutron flux includes the error in ε_γ , statistical and fitting errors in

the photo peak area of 846.7 keV γ -ray (N_γ) and error in the coincident summing correction factor for ^{56}Mn .

Table 3. Estimated energy integrated neutron flux from $^{56}\text{Fe}(n, p)^{56}\text{Mn}$ reaction for different proton energies (at $d \sim 5$ cm).

Production Target	E_p (MeV)	E_{max} (MeV)	$\langle E_n \rangle$ (MeV)	ϕ_n ($n\text{ cm}^{-2}\text{s}^{-1}$)
^9Be	12	9.9	3.9	$2.3(0.2) \times 10^5$
	20	17.9	5.6	$9.9(0.7) \times 10^5$
$^{\text{nat}}\text{Li}$ [26]	12	10.1	9.85	$1.3(0.2) \times 10^5$

3.4.2 Estimation of neutron-induced gamma background for $E_\gamma \geq 2.1$ MeV

Neutron-induced gamma background at energies $E_\gamma \geq 2.1$ MeV is estimated for the measured neutron flux corresponding to $E_p = 20$ MeV. The activity of different reaction products in the $^{\text{nat}}\text{Cu}$, $^{\text{nat}}\text{Pb}$ and $^{124,\text{nat}}\text{Sn}$ samples is calculated with observed γ -rays of 2003.7 keV, 602.7 keV and 416.9 keV, respectively. These γ -rays were visible above the detection limit of the low background setup only in the close geometry. The neutron flux is corrected for solid angle subtended by targets in the cascade geometry, placed at different distances (d) from the production target. The expected yield of the high energy gamma rays, which are potential sources of background for double beta decay studies, is estimated from this activity using known branching ratios and is given in table 4. It should be noted that the coincident summing of low energy gamma-rays in these decay cascades can also produce gamma background in the ROI, which will depend on the detector configuration.

Table 4. Estimated neutron-induced background from the high energy γ -rays in Pb, Cu and Sn samples.

Sample	Neutron fluence $n\text{ cm}^{-2}(\times 10^{10})$	Reaction Product	$T_{1/2}$	E_γ of interest (keV)	Expected Activity of E_γ (Bq g^{-1})
$^{\text{nat}}\text{Pb}$	0.30(2)	^{124}Sb	60.2 d	2182.6	0.0007(3)
				2294.0	0.0005(2)
$^{\text{nat}}\text{Cu}$	0.33(2)	$^{62\text{m}}\text{Co}$	13.91 min	2301.9	6(2)
				2882.3	4(1)
^{124}Sn	1.6(1)	$^{116\text{m}}\text{In}$	54.29 min	2112.3	5(1)
$^{\text{nat}}\text{Sn}$	0.84(6)	$^{116\text{m}}\text{In}$	54.29 min	2112.3	24(6)

Most of the activities producing high energy gamma-rays are short-lived and can be minimized by storage in an underground location prior to use in the detector setup. Typical neutron flux in underground locations at $E_n < 10$ MeV is $10^{-6}n\text{ cm}^{-2}\text{s}^{-1}$ [9] and the required overall background level will be $< 10^{-2}$ counts/(keV kg year). Hence, contribution from Cu and Pb samples in the region of high energy gamma-rays would be negligible. From table 4, it can be seen that $^{\text{nat}}\text{Sn}$ will produce $\sim 5(2)$ times higher gamma background of 2112.3 keV on neutron activation and can be of concern.

4. Conclusions

Neutron-induced background has been studied in various materials to be used in the TIN.TIN detector, which is being developed for the search of $0\nu\beta\beta$ decay in ^{124}Sn . In the present work, materials such as Torlon 4203 and 4301, Teflon, $^{\text{nat}}\text{Cu}$, $^{\text{nat}}\text{Pb}$ and $^{124,\text{nat}}\text{Sn}$ are studied. The contribution to the gamma background has been evaluated for an average neutron flux $\sim 10^6 \text{ n cm}^{-2}\text{s}^{-1}$ integrated over neutron energy $E_n = \sim 0.1$ to ~ 18 MeV. Both Torlon samples show presence of Al which will contribute to high energy gamma background. In addition, Torlon 4301 has Fe impurity while Ti in Torlon 4203 can produce long-lived impurities like ^{46}Sc . Teflon shows only 511 keV γ -ray activity resulting from $^{19}\text{F}(n, 2n)^{18}\text{F}$ reaction at $E_n \geq 11.5$ MeV. Hence, Teflon appears to be a better material for support structures in the Sn cryogenic bolometer from neutron-induced background consideration. Although, the $^{\text{nat}}\text{Cu}$ sample and Sb impurity in $^{\text{nat}}\text{Pb}$ produces high energy gamma background ($E_\gamma > 2.1$ MeV) upon neutron activation, the contribution in the ROI of $0\nu\beta\beta$ decay in ^{124}Sn is estimated to be negligible. The neutron-induced reactions form short-lived activities in both ^{124}Sn and $^{\text{nat}}\text{Sn}$ samples, which are of concern for the Tin detector. Among the various Sn isotopes formed ^{123}Sn has the longest half-life $T_{1/2} = 129.2$ d, while $^{116\text{m}}\text{In}$ produces high energy γ -ray 2112.3 keV within the ROI for $0\nu\beta\beta$ in ^{124}Sn . Thus, for background reduction in the ROI enriched Tin is preferable as compared to natural Tin. Further, these results suggest that it would be necessary to store Sn material in underground location for extended periods prior to use in the cryogenic bolometer setup.

Acknowledgments

The authors would like to thank Mr. S.C. Sharma, Mr. M.S. Pose, Mr. K.V. Anoop and Mr. K.V. Divekar for help during the setup and Mr. A.G. Mahadkar for the preparation of targets. We are grateful to the Pelletron Linac staff for the smooth operation of the machine during the experiment.

References

- [1] A.S. Barabash, *Average and recommended half-life values for two neutrino double beta decay: upgrade 2013*, *arXiv:1311.2421v1* (2013).
- [2] D.R. Artusa et al., *Initial performance of the CUORE-0 experiment*, *Eur. Phys. J. C* **74** (2014) 2956 .
- [3] M. Agostini et al., *Results on Neutrinoless Double- β Decay of ^{76}Ge from Phase I of the GERDA Experiment*, *Phys. Rev. Lett.* **111** (2013) 152203.
- [4] H.J. Kim et al., *Measurement of the neutron flux in the CPL underground laboratory and simulation studies of neutron shielding for WIMP searches*, *Astroparticle Physics* **20** (2004) 549.
- [5] H. Wulandari, J. Jochum, W. Rau, F. von Feilitzsch, *Neutron flux at the Gran Sasso underground laboratory revisited*, *Astroparticle Physics* **22** (2004) 313.
- [6] F. Bellini, C. Bucci, S. Capelli, O. Cremonesi, L. Gironi, M. Martinez, M. Pavan, C. Tomei, M. Vignati, *Monte Carlo evaluation of the external gamma, neutron and muon induced background sources in the CUORE experiment*, *Astroparticle Physics* **33** (2010) 169.
- [7] D.M. Mei and A. Hime, *Muon-induced background study for underground laboratories*, *Phys. Rev. D* **73** (2006) 053004.

- [8] D.M. Mei, S.R. Elliott, A. Hime, V. Gehman and K. Kazkaz, *Neutron inelastic scattering processes as a background for double- β decay experiments*, *Phys. Rev. C* **77** (2008) 054614.
- [9] E. Andreotti et al., *Muon-induced backgrounds in the CUORICINO experiment*, *Astroparticle Physics* **34** (2010) 18.
- [10] C. Bungau, B. Camanzi, J. Champer, Y. Chen, D.B. Cline, R. Luscher, J.D. Lewin, P.F. Smith, N.J.T. Smith, H. Wang, *Monte Carlo studies of combined shielding and veto techniques for neutron background reduction in underground dark matter experiments based on liquid noble gas targets*, *Astroparticle Physics* **23** (2005) 97.
- [11] V. Nanal, *Search for neutrinoless double beta decay in ^{124}Sn* , *EPJ Web of Conferences* **66** (2014) 08005.
- [12] V. Singh, S. Mathimalar, N. Dokania, V. Nanal, R.G. Pillay, S. Ramakrishnan, *Cryogen-free dilution refrigerator for bolometric search of neutrinoless double beta decay ($0\nu\beta\beta$) in ^{124}Sn* , *Pramana* **81** (2013) 719.
- [13] D.A. Nesterenko et al., *Double- β transformations in isobaric triplets with mass numbers $A = 124, 130$, and 136* , *Phys. Rev. C* **86** (2012) 044313.
- [14] C. Arnaboldi et al., *CUORE: a cryogenic underground observatory for rare events*, *Nucl. Instr. Meth. A* **518** (2004) 775.
- [15] R.G. Wilson, *SIMS qualification in Si, GaAs, and diamond - an update*, *International Journal of Mass Spectrometry and Ion Processes* **143** (1995) 43.
- [16] *Torlon Resins Engineering Data*, Solvay Advanced Polymers.
- [17] Sabyasachi Paul, G.S. Sahoo, S.P. Tripathy, S.C. Sharma, Ramjilal, N.G. Ninawe, C. Sunil, A.K. Gupta, and T. Bandyopadhyay, *Measurement of neutron spectra generated from bombardment of 4 to 24 MeV protons on a thick ^9Be target and estimation of neutron yields*, *Rev. of Sci. Instruments* **85** (2014) 063501.
- [18] So Kamada, Toshiro Itoga, Yasuhiro Unno, Wataru Takahashi, Takuji Oishi and Mamoru Baba, *Measurement of Energy-angular Neutron Distribution for ^7Li , $^9\text{Be}(p, xn)$ Reaction at $E_p = 70$ MeV and 11 MeV*, *Journal of the Korean Physical Society* **59** (2011) 1676.
- [19] C.H. Poppe, J.D. Anderson, J.C. Davis, S.M. Grimes and C. Wong, *Cross sections for the $^7\text{Li}(p, n)^9\text{Be}$ reaction between 4.2 and 26 MeV*, *Phys. Rev. C* **14** (1976) 438.
- [20] S.P. Simakov and U. Fischier, *Analysis of the Dosimetry Cross Sections Measurements up to 35 MeV with a $^7\text{Li}(p, xn)$ Quasi-monoenergetic Neutron Source*, *Journal of the Korean Physical Society* **59** (2011) 1856.
- [21] N. Dokania, V. Singh, S. Mathimalar, V. Nanal, S. Pal, R.G. Pillay, *Characterization and modeling of a low background HPGe detector*, *Nucl. Instr. Meth. A* **745** (2014) 119.
- [22] K.V. Anoop, S. Pal, N. Dokania, V. Nanal, R.G. Pillay, *Performance of digitizers with HPGe and scintillation detectors* in proceedings of 58th DAE Symposium on Nuclear Physics, December, 2–6, 2013 Bhabha Atomic Research Center, India.
- [23] Linux Advanced Multi-Parameter System (LAMPS)
- [24] www.nndc.bnl.gov
- [25] V.K. Mulik, H. Naik, S.V. Suryanarayana, S.D. Dhole, P.M. Prajapati, B.S. Shivashankar, K.C. Jagadeesan, S.V. Thakre, V.N. Bhoraskar and A. Goswami, *Measurement of $^{56}\text{Fe}(n, p)^{56}\text{Mn}$ reaction cross-section at $E_n = 5.9, 9.85, 14.8$ and 15.5 MeV*, *J. of Radioanal. Nucl. Chem.* **296** (2013) 1321.

- [26] H. Naik et al., *Measurement of the neutron capture cross-section of ^{232}Th using the neutron activation technique*, *Eur. Phys. J. A* **47** (2011) 51.
- [27] D.S. Akerib et al., *Radio-assay of Titanium samples for the LUX Experiment*, *arXiv:1112.1376v3* (2012).
- [28] D.S. Akerib et al., *Radiogenic and Muon-Induced Backgrounds in the LUX Dark Matter Detector*, *arXiv:1403.1299v1* (2014)
- [29] J. Argyriades et al., *Measurement of the background in the NEMO 3 double beta decay experiment*, *Nucl. Instr. Meth. A* **606** (2009) 449.